Enhanced performance polyamide membrane by introducing high-porosity SOD/GO composite interlayer to tailor the interfacial polymerization process

S. C. Wei, X. C. Ding, Y. Qiu, Vincent de Waele, H. L. Guo

Enhanced performance polyamide membrane by introducing high-porosity SOD/GO composite interlayer to tailor the interfacial polymerization process

Shengchao Wei[a], Xuechun Ding[a], Yu Qiu[b], Vincent De Waele[c], Hailing Guo[a*]

[a] State Key Laboratory of Heavy Oil Processing, College of Chemical Engineering, China University of Petroleum (East China), Qingdao 266580, China.

[b] Fujian Jinhuang Environmental Protection Technology Co., Ltd, 350002 Fujian, PR China

[c] UMR 8516, LASIRE-Laboratoire de Spectroscopie Pour Les Interactions, La Réactivité et L'Environnement, Univ. Lille, CNRS, 59000, Lille, France

* Corresponding author.

Hailing Guo's Email: guohl@upc.edu.cn

ABSTRACT

Controllable preparation of high-performance polyamide nanofiltration (NF) membranes that can be used in various applications such as seawater desalination and wastewater treatment is very promising. In this work, a high-performance polyamide NF membrane was designed using high-porosity hydroxy sodalite/graphene oxide (SOD/GO) composite interlayer to slow down the diffusion of amine monomer and control the interfacial polymerization (IP) process. The unique tortuous effect and hydrogen bonds with amine monomers caused by the dense interlayer significantly inhibit the diffusion of amine monomers (reduction of 50% in diffusion rate), thereby resulting in the controllable slow IP process. The slowing IP process facilitates the formation of thinner dense polyamide (PA) layer with stripe morphology and narrow pore size. Consequently, the optimal polyamide membrane with composite interlayer possesses a superior water permeability of 22.05 L m^{-2} h^{-1}·bar^{-1}, nearly 2.5 fold that of the controlled one, while retaining an excellent rejection of Na_2SO_4 (97.25±0.81%). Moreover, the polyamide membrane depicts outstanding antifouling propensity (flux-recovery ratio (FRR)=82%), long-term stability (80 h) and pressure resistance (9 bar). This work provides a novel strategy for controllable construction of high-performance NF membrane and deepens the slights into the interlayer influences IP process.

KEYWORDS

Nanofiltration membrane; Interfacial polymerization; Interlayer; GO nanosheets; Zeolite

1. Introduction

Membrane separation technology, due to its high separation efficiency and low energy consumption, has great development prospects in seawater desalination and wastewater treatment [1-3]. Among the membrane "family", nanofiltration (NF) membrane plays a crucial role due to its unique separation properties (rejecting multivalent salt ions and organic molecules) and application advantages (low cost, easy operation, and scalability) [4-6]. Currently, the thin-film composite (TFC) NF membrane fabricated through the interfacial polymerization (IP) of piperazine (PIP) and trimesoyl chloride (TMC) on porous substrates has achieved significant success and dominated the NF membrane market [4, 7, 8]. Nevertheless, the IP process of PIP and TMC monomer is quite fast and uncontrollable, which results in the inhomogeneous pore size and unfavorable thickness for the polyamide (PA) selective layer in TFC NF membrane, leading to the "trade-off" that permeance and ion selectivity cannot be improved at the same time [9].

The separation performance of TFC membranes is closely associated with the structural properties of the PA layer [10, 11]. In the past few years, various strategies have been implemented to tailor the IP reaction and optimize the structure of PA separation layer with desirable performance, including changing the reaction monomer [12-15], surface modification [16-19], introducing additives into aqueous or organic phase [2, 11, 20-23], optimizing the operation condition [24-26], and fabricating interlayer [10, 27-29]. Among them, fabricating interlayer between PA layer and substrate has been proven to be an effective strategy for controlling the IP process and improving membranes' performance [30]. The interlayer can

regulate the surface properties and pore structure of substrate, optimizing the storage, release, and diffusion of PIP monomers on substrate and modulating the formation of PA layer [10, 30]. Currently, various nanomaterials were employed as an interlayer in TFC NF membranes, including TiO_2 [31, 32], carbon nanotube [33, 34], GO [35, 36], metal-organic frameworks [37, 38], zeolite [39], etc. Despite these hydrophilic nanomaterials can optimize the storage of amine monomers on substrate, they have unavoidable limitations in regulating the diffusion of amine monomers due to their limited space, so the IP process still was rather rapid [40]. And the rapidity and complexity of the IP reaction caused the mechanism of membrane structural properties regulated by the interlayer has not been clearly revealed.

Recently, graphene oxide (GO) nanosheets have attracted wide interest in NF membranes due to their excellent hydrophilic and the "tortuous effect" on the diffusion of loaded molecules [41-43]. Tian et al fabricated a thinner PA layer in TFC membrane with enhanced water permeance (an increase of 57%) by introducing the GO interlayer [44]. Lau et al constructed a high-performance TFC NF membrane (the water permeance was 31.4% higher than that of controlled one) by inserting GO nanosheets on substrates to improve the hydrophilicity of membranes [36]. Nevertheless, these stacked GO nanosheets are susceptible to being compacted and exhibit poor structural stability [45]. Inserting porous nanomaterials into the stacked GO interlayer is promising for improving the space of interlayer and enhancing the stability of interlayer, thereby controllable tailoring the IP reaction by optimizing the storage and diffusion of amine [46]. In addition, the larger pores of nanomaterials/GO composite interlayer provide more free volume to the PA layer, which facilitates mass transfer [47].

Ultrasmall zeolite nanocrystals have great potential in modulating GO interlayer structures and improving membrane performance due to their unique structural properties (ultrasmall size, porous structure, silanol-rich, and high surface energy) [48, 49]. Introducing zeolite crystal as an additive or interlayer in TFC NF membrane achieves a substantial increase in membrane permeability as reported in our previous studies [39, 50]. Meanwhile, the silica hydroxyl groups of zeolite nanocrystals can promote the formation of hydrogen bonds with the GO nanosheets to enhance the stability of zeolite/GO composite materials [51].

In this work, a novel interlayer-based thin-film composite (i-TFC) membrane possessing stripe structure was designed by incorporating a high-porosity hydroxy sodalite/graphene oxide (SOD/GO) composite interlayer to control the IP process. The composite SOD/GO interlayer can reduce significantly the diffusion of amine monomer due to the strong interaction with amine monomers and the tortuous effect, causing that the IP process is controllable and homogeneous. Due to the optimal structure (stripe structure, thinner, and dense) of the PA layer and low-resistance water transfer path, the introduction of SOD/GO composite interlayer increased the water permeance (2.5-fold water permeance of the control one) and salts rejection of i-TFC membranes. Moreover, the composite SOD/GO interlayer endows the membrane with outstanding long-term stability and anti-fouling ability. Such membranes with SOD/GO interlayer provides a new approach to designing high-performance TFC NF membranes.

2. Experimental section

2.1. Materials

The colloidal silica (LUDOX HS-30, 30 wt%, pH=9.8) was purchased from Sigma-Aldrich and aluminum powder (325 mesh, 99.5%, metal basis) was obtained from Alfa Aesar. Sodium hydroxide (NaOH, AR, ≥97%), n-hexane (AR, ≥97%), Na_2SO_4 (AR, ⩾99%), $MgSO_4$ (AR, ⩾98%), $MgCl_2·6H_2O$ (AR, ⩾99%), $CaCl_2$ (AR, ⩾99%), NaCl (AR, ⩾99%), and Polyethylene glycol (PEG, CP, molecular weight: 200, 300, 400, 600, 8000, 20000, 70000, 100000, and 200000) were provided from Sinopharm Chemical Reagent Co., Ltd (China). Graphene oxides (GO) were purchased from XFNANO Materials Tech Co. Ltd (Nanjing). Polyethersulfone microporous membranes (PES, pore diameter: 100 nm) were acquired from Haiyan Xindongfang Suhua Co., Ltd. The monomer piperazine (PIP, ≥98%) and trimesoyl chloride (TMC, ≥98%) were obtained from TCI (Shanghai). The deionized (DI) water was supplied using a two-stage RO device.

2.2. Preparation of SOD zeolite crystals

Based on the previous study [52], the synthesis procedures was carried out as follows: 5 g of NaOH was dissolved in 10 g of DI water followed by a dropwise addition of 0.54g of Al powder (denoted as solution Al). 9.37 g of NaOH was dissolved in 16 g of DI water, which was then added dropwise to 10 g of colloidal silica (30 wt%) with stirring. After the solution was stirred until clarified, 10.20 g of DI water was added slowly to the solution (denoted as Solution

113 Si). Next, the as-prepared solution Si and solution Al were kept in ice water. Under cooling and
114 stirring vigorously, the solution Al was added dropwise to the solution Si to forming the discrete
115 amorphous particles and ensure the formation of ultrasmall zeolite [53]. Then the resulting
116 suspension was stirred and kept for 24 h at 25°C. After that, the suspension was moved into the
117 oven at 60°C for 48 h. The crystallized products (denoted as SOD zeolites) were isolated by
118 centrifugation (12000 rpm, 20 min) repeatedly until the decanting solution reached a pH of 8.
119 The SOD aqueous solution (0.1 wt%) was obtained by wet dispersion method (avoiding the
120 aggregation of the SOD nanocrystal). The centrifuged supernatant was obtained by
121 centrifugating (12000 rpm, 20 min) the above SOD aqueous solution as SOD aqueous
122 dispersion.

123 *2.3. Fabrication of i-TFC NF membrane with SOD/GO interlayer*

124 The SOD/GO interlayers were constructed on substrates by vacuum filtration SOD/GO
125 aqueous solutions. As illustrated in Fig. 1, 2.5 g of GO aqueous solution (0.001wt%) was mixed
126 with different amounts (3 g, 6 g, and 9 g) of SOD aqueous dispersion by sonication in an ice-
127 water bath, which was then diluted the solution to 18 g with DI water. And the mixed SOD/GO
128 aqueous solution was further sonicated for 1 h to promote dispersion. The SOD/GO composite
129 interlayers on the substrate were constructed via vacuum-filtering dispersed SOD/GO aqueous
130 solution onto the PES substrate (area of 12.56 cm^2) under a low filtering pressure (0.02 MPa).
131 Subsequently, the as-constructed SOD/GO interlayers were moved into the oven at 60°C for 5
132 min to remove the residual water. The modified PES-SG substrates with different SOD amounts

(3 g, 6 g, and 9 g) in SOD/GO interlayers were denoted as PES-SG-3, PES-SG-6, and PES-SG-9 substrates, respectively.

As depicted in Fig. 1, the i-TFC membranes were constructed on the PES-SG modified substrates via IP reaction of PIP and TMC. Firstly, the PIP aqueous solution (0.2 wt%) was contacted with the surface of PES-SG modified substrates for 5 min, followed by removing the excess PIP solution via the roller. After that, the TMC/n-hexane (0.15 wt%) was poured on the surface of substrate to initiate the IP reaction. After reacting for 1 min, the obtained membranes were washed with n-hexane for 8 s and heated at 60°C for 20 min using the oven. All the constructed membranes were stored in DI water. The membranes were constructed on the PES-SG-3, PES-SG-6, and PES-SG-9 were denoted as i-TFC-SG-3, i-TFC-SG-6, and i-TFC-SG-9, respectively. The membrane constructed on the PES substrate was denoted as the TFC membrane, as the controlled one.

2.4. Separation performance of as-fabricated membranes

The ionic sieving ability of fabricated membranes was investigated on a crossflow equipment with 7.065 cm^2 cells. During the test, the filtrating pressure was 3 bar. The different inorganic salt aqueous (2000 μg/g) were separated as the feed, including Na_2SO_4, $MgSO_4$, $MgCl_2$, $CaCl_2$, and NaCl. Before collecting the permeate water, the membranes were pre-pressurized at 3 bar for 2 h. The salt solutions' concentrations were determined via the conductivity meter. The salts rejections (R) of membranes were calculated based on Eq. (1)[12].

$$R = \left(1 - \frac{C_P}{C_f}\right) \times 100\% \quad (1)$$

153 Where C_p stands for the salt's concentration of permeate and the C_f is the salt's concentration
154 of feed. The permeance (J_w, L) of the membrane was calculated by the Eq. (2).

155 $$Jw = \frac{Q}{P\,\Delta t\,A} \quad (2)$$

156 Of which Q (L) and A (m^2) are the permeate volume and testing area of the membrane,
157 respectively. P (bar) and Δt (h) are the testing pressure and time, respectively.

158 The pore structure of the fabricated membrane was acquired by solute transport methods [54].
159 In brief, the rejection curves of PEG for the fabricated membranes were measured via filtrating
160 five PEG solutions (200 μg/g) with different molecular weights (200, 300, 400, and 600 Da) on
161 Eq. (3). The total organic carbon analyzer was used to determine the concentration of PEG
162 solution. The MWCO of the membrane was the molecular weight corresponding to the 90%
163 rejection.

164 $$R_{PEG} = \left(1 - \frac{TOC_P}{TOC_f}\right) \times 100\% \quad (3)$$

165 The R_{PEG}, TOC_p *and* TOC_f are PEG rejection, the PEG concentration of permeate and
166 feedstock, respectively. The molecular stokes diameter (d_s, nm) was acquired on Eq. (4).

167 $$d_s = 33.46 \times 10^{-3} \times M^{0.557} \quad (4)$$

168 *2.5. Antifouling filtration test*

169 The BSA solution (200 μg/g) was employed to explore the antifouling ability of the
170 constructed membranes. The membranes were pre-pressurized at 3 bars for 2 h to acquire a
171 stable water flux (denoted as F_0, L m^{-2} h^{-1}). After that, the DI water and BSA solution were
172 alternatively filtrated. It must be noted that the membrane and cell must be thoroughly cleaned

with DI water repeatedly after testing with the BSA solutions to remove the contaminants onto the membrane surface. The membrane flux at the final filtration cycle was denoted as F_1 (L m^{-2} h^{-1}). The flux-recovery ratio (FRR) for the membrane was obtained by Eq. (5).

$$FRR = \frac{F_1}{F_0} \times 100\% \quad (5)$$

2.6. Characterizations

The crystallinity of the zeolites was investigated by XRD (Bruker D8 Advance, USA). The vibrational properties and crystal size of SOD zeolites were investigated by FTIR (Bruker Vertex, USA) and TEM (Tecnai F20, USA), respectively. The thermal stability of SOD zeolite was explored on a Thermogravimetric-mass spectrometry (TG-MS, Netzsch STA 449F5, Germany). The N_2/H_2 adsorption/desorption isotherm (Micromeritics ASAP 2020, USA) was performed to determine the porosity of SOD zeolite and SOD/GO composite material. The vibrational properties of membranes were determined by FTIR (FTIR, Bruker Vertex, USA), Raman spectroscopy (inVia Reflex, UK) and XPS (Thermo Fisher Scientific, USA). The morphology and roughness of membranes were studied by SEM (JEOL-7900F, Japan) and AFM (Shimadzu SPM-9700, Japan). The surface wettability of samples was investigated on a drop shape analyzer (Krüss DSA25, Germany). The surface charge properties of samples were explored using the streaming potential analyzer (Aaton-Paar SurPASS3, Austria). UV-vis absorption spectra of PIP solutions were investigated on a UV-vis spectrophotometer (SPECORD 210 PLUS, Germany).

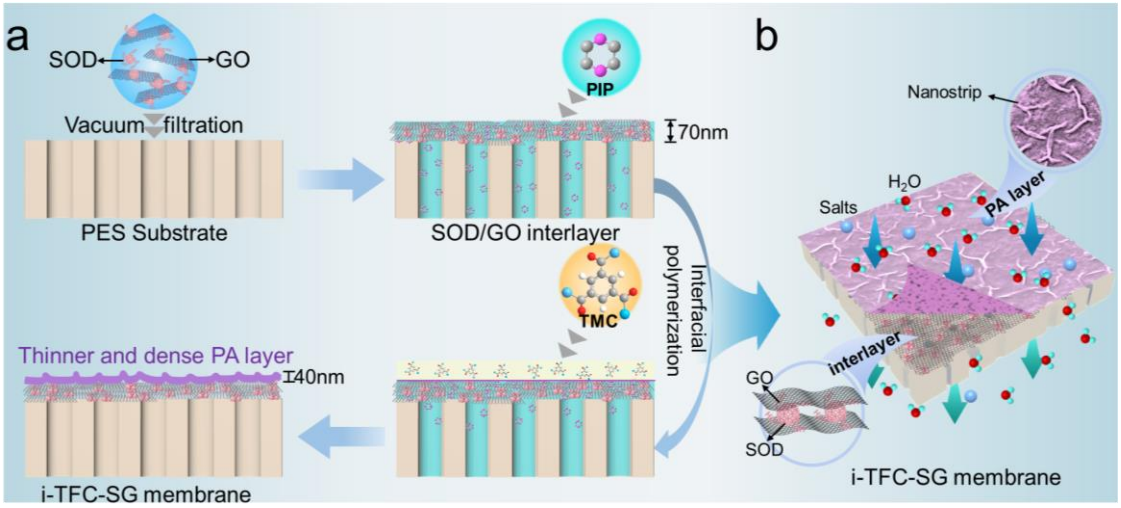

Fig. 1. (a) Preparation procedure of i-TFC-SG membrane. (b) the structure of i-TFC-SG membrane.

3. Results and discussions

3.1. Characterization of SOD zeolite

The XRD pattern of SOD zeolite contains multiple Bragg peaks at 14.14°, 20.06°, 24.62°, 31.96°, and 35.10° corresponding to the SOD-type zeolite structure, which shows the SOD zeolite was successfully synthesized(Fig. 2a) [55]. The synthesized SOD zeolite has a crystal size of about 40 nm, which was demonstrated by the TEM and SEM results as presented in Fig. 2b and Fig. S1. In Fig. S2, the in-situ FTIR spectra of SOD crystals exhibit the signature of the OH stretching mode due to the structural OH bond and the adsorbed water molecules (identified at 1651 cm^{-1}). Upon dehydration by increasing the temperature, the spectra show clearly the structural vibrations v(Si-OH) =3726 cm^{-1}, which facilitates the formation of interactions with the GO nanosheets containing abundant oxygen-containing groups (Fig. S3) [52, 56]. From the BET measurements (Fig. S4), the SOD zeolites exhibit the expected low surface of

microporosity (S_{micro}=15.68 m^2 g^{-1}) of SOD type of framework and large mesopores (S_{meso}=80.47 m^2 g^{-1}) [55]. Fig. S5 exhibits that SOD zeolite has a low Si/Al ratio of 1.05 and a high Si/Na ratio of 0.91. The SOD zeolite is high hydrophilic with a small water contact angle (15-16°) of the SOD zeolite surface. Consequently, the SOD aqueous solution stays clear-water after standing for 48 h (Fig. S6). Besides, the SOD zeolite also exhibits excellent thermal stability (Fig. S7).

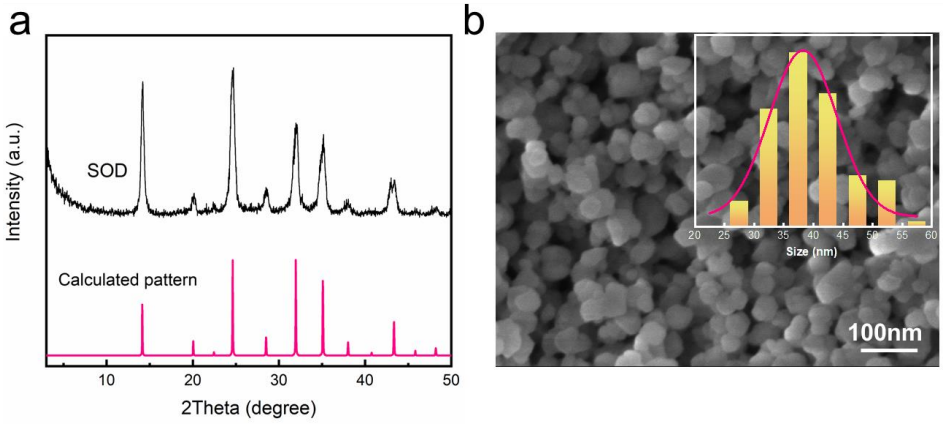

Fig. 2. (a) XRD pattern, (b) SEM image of nanosized SOD zeolite

3.2. Characterization of composite SOD/GO interlayers

As shown in Fig. 3, the pristine PES substrate exhibits a large number of uneven micropores (100-300 nm). In contrast, the PES-SG substrates with SOD/GO composite interlayer exhibit the inter-stacked SOD nanocrystals and GO nanosheets, and the large irregular pores of substrates were covered by the continuous SOD/GO interlayer (Fig. 3a1-d1). The surface arithmetic average roughness (Ra) of PES-SG-3, PES-SG-6, and PES-SG-9 substrates decreased from 30.45 nm to 18.67 nm, 26.72 nm, and 27.50 nm, respectively (Fig. 3a2-d2). The results suggest that the introduced SOD/GO composite interlayer covered the original surface feature of substrate and caused a smooth surface (Fig. S8). Moreover, as seen in Fig. 3a3-d3,

the SOD/GO composite interlayers possess a continuous dense structure. As the amount of SOD zeolite is elevated in the composite SOD interlayer, the thickness of the composite interlayer increases from 52±4 nm to 93±7 nm. These results illustrate that the SOD/GO composite interlayer can reduce the pore size and the surface roughness of substrates.

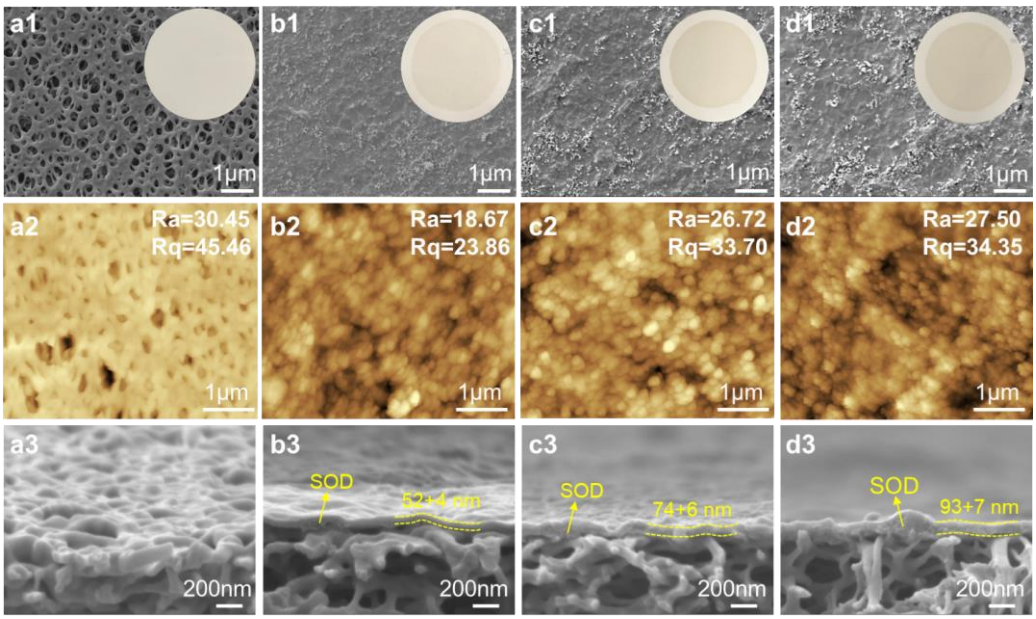

Fig. 3. SEM image of (a1) PES, (b1) PES-SG-3, (c1) PES-SG-6, and (d1) PES-SG-9 substrates, AFM 2D image of (a2) PES, (b2) PES-SG-3, (c2) PES-SG-6, and (d2) PES-SG-9 substrates, SEM cross-sectional image of (a3) PES, (b3) PES-SG-3, (c3) PES-SG-6, and (d3) PES-SG-9 substrates.

All modified PES-SG substrates presented new adsorption peaks at 3400 and 1642 cm^{-1}, which corresponds to the OH stretching vibration and deformation of water (Fig. 4a). In the Raman spectra (Fig. 4b), the modified PES-SG membranes exhibits a D band (1350 cm^{-1}) and a G band (1600 cm^{-1}), which were assigned to the GO nanosheets [57]. As shown in Fig. S9, the water contact angle (WCA) of the modified substrates reduced from 38° (PES) to 33° (PES-SG-6). The decrease in the WCA of the PES-SG substrates proves that the composite SOD/GO

interlayer improved the surface hydrophilicity of substrates. And the increased amount of SOD zeolite in composite SOD/GO interlayer can further increase the surface hydrophilicity of PES-SG substrates. Fig. S10 exhibit the chemical composition of PEG-SG substrates using SEM-Mapping. As shown, the silicon and carbon elements are evenly distributed on the PEG-SG substrates, suggesting that the uniform distribution of SOD zeolite and GO nanosheets. Fig. S11 shows that the surface of the PES substrate was negatively charged (zeta potential was -30 mV at pH=7), while the PES-SG-6 substrate has a lower zeta potential (-43 mV) at pH=7 due to the carboxy and hydroxyl groups in the SOD/GO composite interlayer. Moreover, the SOD/GO composite interlayer possesses abundant inter-crystalline mesopores (V_{meso}=0.3467 cm^{-3} g^{-1}) and micropores, which was determined by the BET (Fig. S12). The MWCO and effective pore size of the PES substrate and PES-SG substrates were determined by solute transport method and presented in Fig. 4c [54]. After inserting SOD/GO composite interlayer, the MWCO and effective pore size of PES-SG substrates decreased significantly, which suggests that the interlayer can narrow the surface pore of the substrates. Compared with that of PES substrate, the water permeance of PES-SG-6 substrates decrease from 424 $L \cdot m^{-2} \cdot h^{-1} \cdot bar^{-1}$ to 249 $L \cdot m^{-2} \cdot h^{-1} \cdot bar^{-1}$ due to the reduction of the surface pore size of the PES-SG substrates (Fig. S13). The composite SOD/GO interlayer could provide a more narrowed pore size and hydrophilic reaction interface with negative charge for the IP reaction.

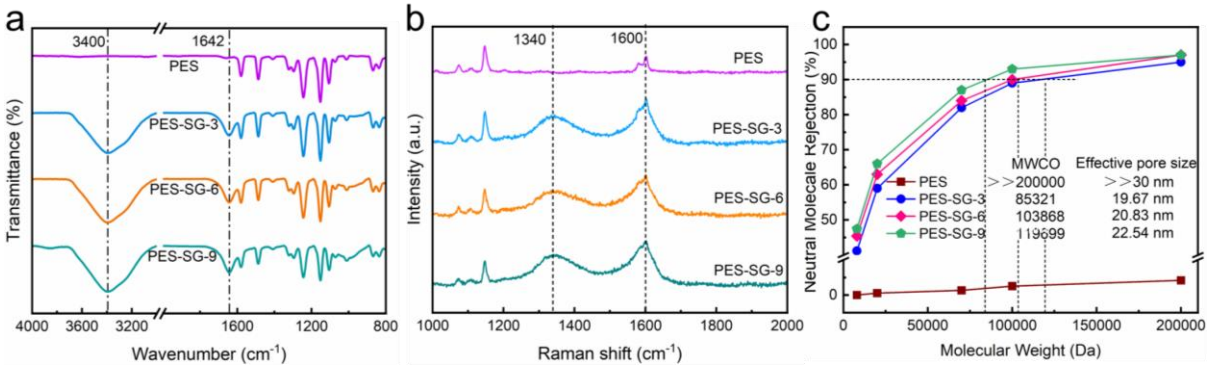

Fig. 4. (a) ATR-FTIR spectra and (b) Raman spectra of PES and modified PES-SG substrates, (c) PEG rejection curves, MWCO, and effective pore size of the PES substrate and modified PES-SG substrates

3.3. Physiochemical properties of NF membranes

As shown in Fig. 5a, a new sharp peak at 1620 cm^{-1} ascribed to the stretching vibration of C=O and N-H of the amide groups (N-C=O) appeared on the ATR-FTIR spectra of the TFC and i-TFC-SG membranes compared to the PES substrates [22]. Notably, the i-TFC-SG membranes possessing composite SOD/GO interlayer have an enhanced peak intensity of amine groups, which suggests that the PA layer of i-TFC-SG membranes contains a higher content of amide groups. As presented in Fig. 5b, c, the O/N ratio of the PA layer for i-TFC-SG membranes reduced compared to the controlled one, displaying the cross-linking degree of the PA layer increased. After inserting composite SOD/GO interlayer with different SOD zeolite amounts, the cross-linking degree of i-TFC membranes increased from 39.1% of TFC to 42.9% of i-TFC-SG-3, 50.5% of i-TFC-SG-6, and 52.7% of i-TFC-SG-9. Compared to that of pristine substrate, the high-porosity SOD/GO composite interlayer provides more PIP monomers to participate in the IP reaction and exhibit unique mass transfer behavior, which makes the IP process controllable.

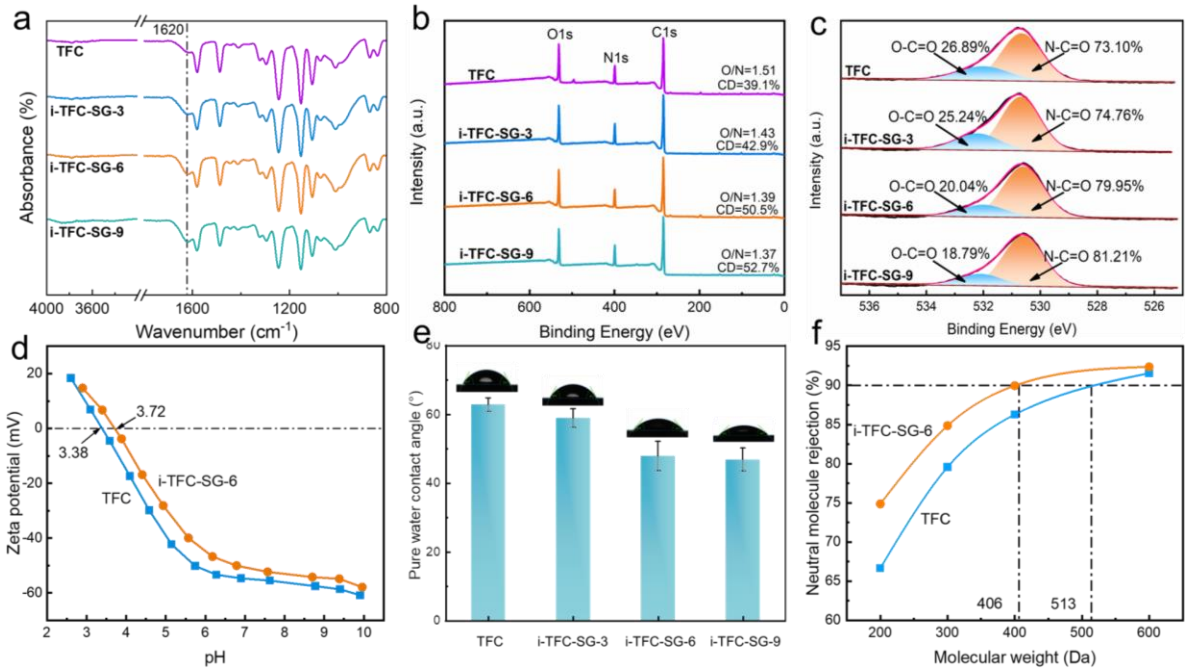

Fig. 5. (a) ATR-FTIR spectra, (b) XPS survey, (c) O1s XPS survey, (d) Surface zeta potentials, (e) Water contact angles, and (f) MWCO of TFC and i-TFC-SG membranes.

As exhibited in Fig. 5d, the i-TFC-SG-6 membrane exhibits a higher isoelectric point (IEP=3.72) than that of the controlled TFC membrane (IEP=3.38), which indicates that the composite interlayer decreased the electronegativity of membrane. And the variation of electronegativity of the i-TFC-SG membranes may be due to its higher content of amide groups of PA layer. Moreover, as presented in Fig. 5e, compared with that of TFC membrane (CA=62.8°), the water contact angle of i-TFC-SG-3 (CA=58.8°), TFC-SG-6 (CA=47.88°), and TFC-SG-9 (CA=46.7°) membranes decreased. Inserting the composite SOD/GO interlayer enhances the hydrophilicity of i-TFC-SG membrane, which was ascribed to the PA layer with more amide groups and the introduction of high-hydrophilic SOD/GO interlayer. In Fig. 5f, the i-TFC-SG-6 membrane has a lower MWCO (406.6) than that of the controlled TFC membrane (513.9), which suggests that the i-TFC-SG-6 membrane with composite SOD/GO interlayer has a small effective pore size. Inserting composite SOD/GO interlayer reduces the effective

pore size and enhances the cross-linking degree of the PA layer by regulating the IP process.

3.4. Surface morphologies of NF membranes

As evident in Fig. 6a1, the pristine TFC membrane possesses a typical nodular morphology, and part of the polyamide grows downward near the macropores of the substrate. After inserting the pure GO interlayer and SOD/GO composite interlayer, the downward growth of polyamide was inhibited (Fig. S14 and Fig. 6a1-d1). Notably, some unique nanostrip structures arose on the surface of i-TFC-SG membranes, and the i-TFC-SG-6 membrane possesses uniform dense nanostrips morphology. As the SOD zeolite amount in composite interlayer elevated, the nanostrip structures in the i-TFC-SG membrane surface became larger and even folded, which are conductive for improving the efficient filtration area of the PA layer [27]. The generation of stripe structure of PA layer was ascribed to the diffusion-driven instability of amine monomer after inserting the SOD/GO composite interlayer [27].

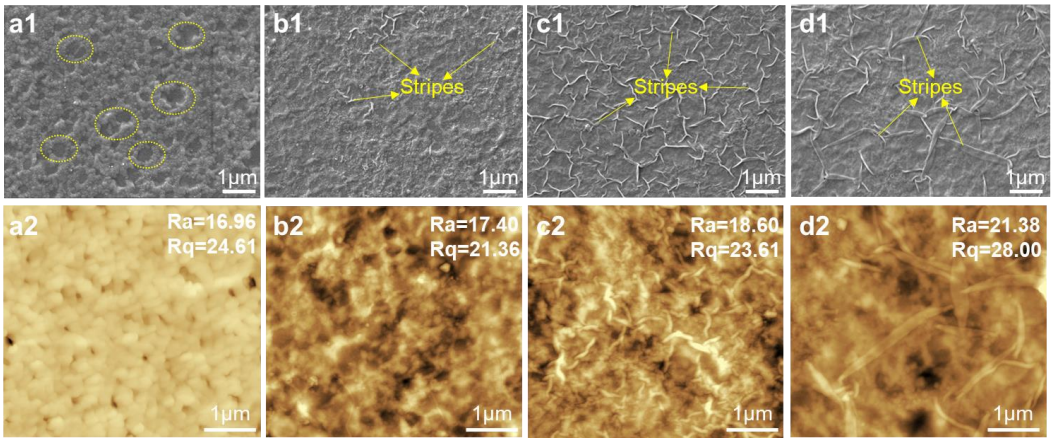

Fig. 6. SEM images of (a1) TFC, (b1) i-TFC-SG-3, (c1) i-TFC- SG-6, and (d1) i-TFC-SG-9 membranes, AFM 2D images of (a2) TFC, (b2) i-TFC-SG-3, (c2) i-TFC- SG-6, and (d2) i-TFC-SG-9 membranes.

306 Moreover, the pristine TFC membrane possesses a lower value of Ra (16.96 nm), indicating
307 it has a smoother surface (Fig. 6a2). After introducing composite SOD/GO interlayer, the value
308 of Ra for the i-TFC-SG-3, i-TFC-SG-6, and i-TFC-SG-9 increase to 17.40 nm, 18.60 nm, and
309 21.38 nm, respectively (Fig. 6a2-d2, Fig. S15). The composite SOD/GO interlayer increases
310 the surface roughness of the membranes by regulating their surface morphology. And the
311 increased surface roughness of i-TFC-SG membranes is beneficial for increasing their efficient
312 filtration area.

313 *3.5. Effect of SOD/GO composite interlayer on IP process*

314 In Fig. 7a-d, the thickness of PA layer for the controlled TFC membrane was 80±3 nm. In
315 contrast, the PA layer's thickness of i-TFC-SG-6 membrane decreased from 80±3 nm to 37±
316 4 nm. As revealed in the Freger equation [58], the increased storage of PIP and decreased
317 diffusion of PIP caused by the SOD/GO composite interlayer jointly led to forming the thinner
318 PA layer. And the reduction of PA layer's thickness in i-TFC-SG membrane can shorten the path
319 of water transport through the membrane.

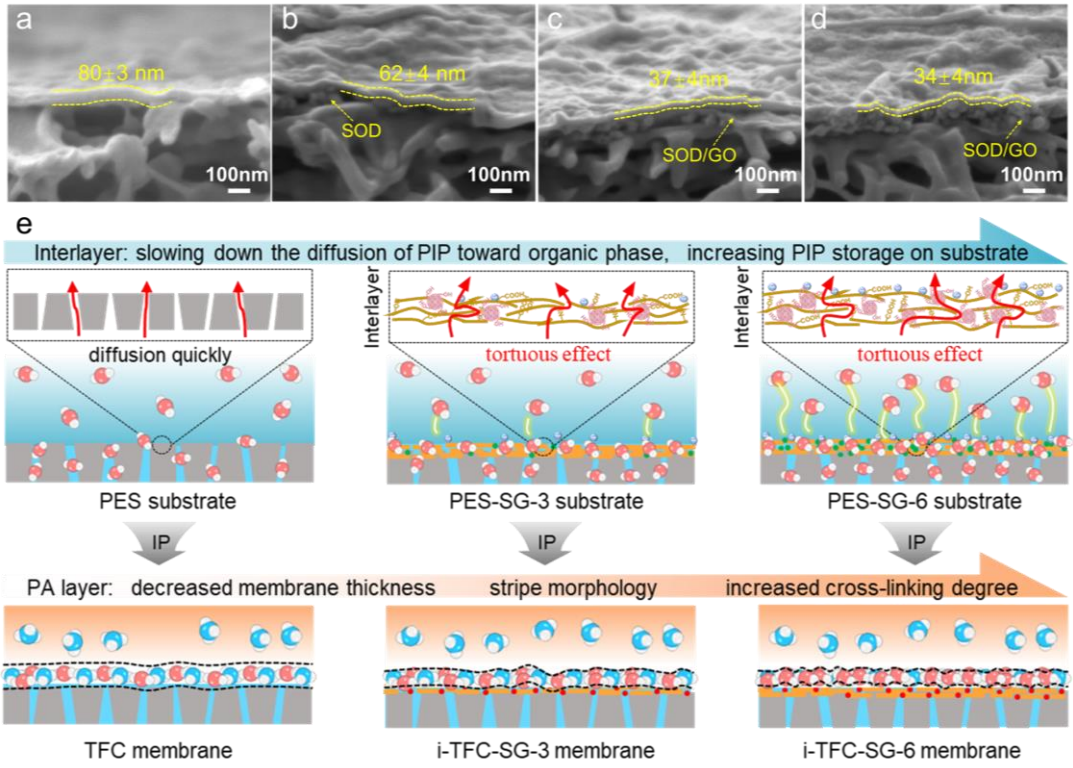

Fig. 7. SEM cross-sectional images of (a) TFC, (b) i-TFC-SG-3, (c) i-TFC-SG-6, and (d) i-TFC-SG-9 membranes, (e) Mechanism diagram of the impact of SOD/GO interlayer on the IP process and the structure of membrane.

The mechanism of the structure of PA layer and IP reaction regulated by the SOD/GO composite interlayer was presented in Fig. 7e. Compared with that of pristine substrate with uneven micropores, the PIP monomers were more evenly distributed on the interlayer's surface, suggesting the diffusion of amine monomers is more homogeneous. The PIP monomers stored in the pristine substrate diffused directly to the interface and reacted with the TMC monomers. For important, the SOD/GO composite interlayer with a large aspect ratio can restrict the diffusion of PIP monomers distributed in interlayers due to the unique "tortuous effect" and the hydrogen bonding interaction with PIP monomers [40]. The limited diffusion behaviors of PIP monomer on interlayer were simulated and determined by H-type diffusion cell (Fig. S16). As

presented in Fig. 8, the intensity of the UV-vis adsorption peak of PIP in n-hexane through the SOD/GO composite interlayer is lower than that of the PIP through the pristine substrate at the same diffusion time. The results demonstrate that the SOD/GO composite interlayer can slow down the diffusion of PIP monomer from aqueous phase to the organic phase. The slope for linear relationship between diffusion time and UV-vis absorption peak intensity of PIP through SOD/GO interlayer and pristine substrate were 0.0333 and 0.0162, respectively. And the results proves that the diffusion rate of PIP monomer is reduced by more than 50% after inserting interlayer. The reduced diffusion of PIP facilitates the homogeneous and controllable IP process, leading to the generation of PA layer with high performance.

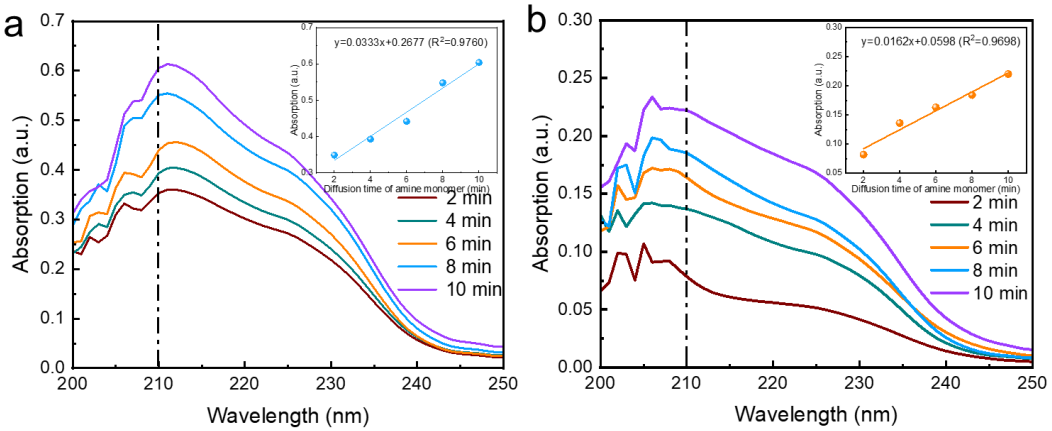

Fig. 8. UV-vis spectra of PIP n-hexane solution that PIP monomers diffused from aqueous solution towards n-hexane through (a) PES or (b) PES-SG-6 substrate with different diffusion times (2, 4, 6, 8, and 10 min), The inserted graph was the linear relationship between diffusion time and absorption peak intensity at 210 nm.

3.6 Separation performance of NF membranes

As presented in Fig. 9a, the TFC membrane has a pure water permeance (PWP) of 8.87 ± 0.51 $L \cdot m^{-2} \cdot h^{-1} \cdot bar^{-1}$ and a Na_2SO_4 rejection of 96.1%. After inserting composite SOD/GO

interlayer, the i-TFC-SG-6 membrane depicts a 2.5-fold PWP (22.05 ± 1.50 $L \cdot m^{-2} \cdot h^{-1} \cdot bar^{-1}$) of the control TFC membrane with a slight increased Na_2SO_4 rejections (97.0%) due to its thinner interlayer (38 nm) and PA layer (76 nm). Meanwhile, increasing the SOD zeolite amount in composite SOD/GO interlayer can increase the PWP without sacrificing their Na_2SO_4 rejections. As depicted in Fig. 9b, all fabricated membranes exhibit a higher retention ability of divalent ions than that of monovalent salts (Na_2SO_4 > $MgSO_4$ > $MgCl_2$ > NaCl), which is consistent with the classical negatively charged TFC membrane [59]. The increased ion selectivity was due to the increased cross-linking degree of the PA layer in i-TFC-SG membranes. And the enhanced water permeance of the i-TFC-SG membranes could be attributed to the rougher membrane surfaces, reduced membrane thickness, and shortened water channels due to the composite SOD/GO interlayer as shown in Fig. 9c.

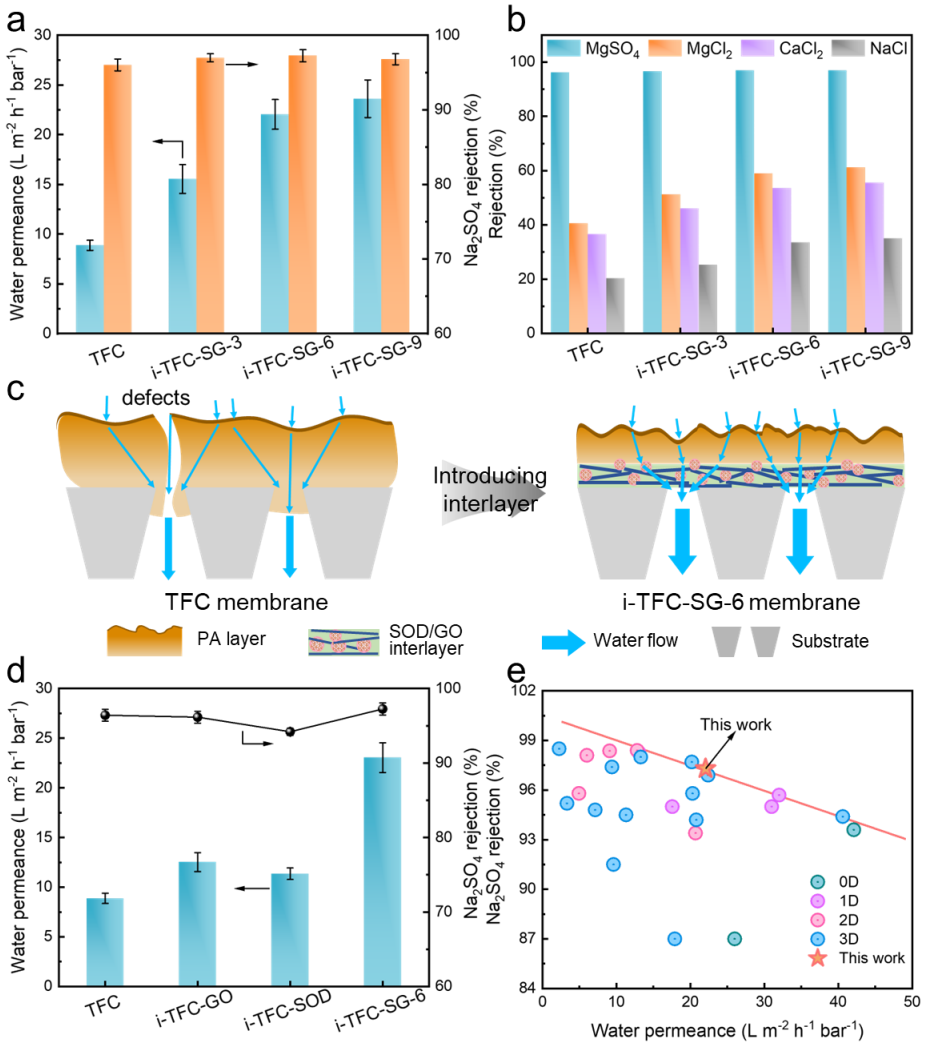

Fig. 9. (a) Membrane separation performance of fabricated membranes, (b) Various salts rejection of fabricated membranes, (c) Mechanisms of increased separation performance of i-TFC-SG membrane using composite SOD/GO interlayer, (d) Membrane separation performance of various NF membranes with different interlayer (pure GO interlayer, pure SOD interlayer), (e) Membrane separation performance of i-TFC-SG-6 membrane with other advanced NF membranes (The relative references were listed in Table S1)

Furthermore, as presented in Fig. 9d, single GO nanosheets as interlayer slightly increased the membrane permeance and selectivity, whereas single SOD zeolites as interlayer resulted in a decrease in membrane selectivity due to its aggregation tendency. In contrast, the composite SOD/GO interlayer with rich-pore structure endows the membrane with excellent water

permeance and selectivity. The desalination performance of the i-TFC-SG-6 membrane and other NF membranes with single nanomaterial interlayer (pure SOD zeolite and pure GO nanosheets) was presented in Fig. 9e. As shown, the i-TFC-SG-6 membrane depicts an outstanding water permeance and Na_2SO_4 rejection in comparison of other advanced NF membranes. The comparative results illustrate that the introduction of composite SOD/GO interlayer in i-TFC membrane is favorable for solving the trade-off effect.

3.7 Anti-fouling performance and long-term stability of NF membranes

As depicted in Fig. 10a, the water fluxes for the fabricated membranes reduced under filtrating BSA solution due to the accumulation of contaminants on the surface of membrane [60]. The i-TFC-SG-6 membrane exhibits a higher FRR (82%) than that of the controlled one (68%), suggesting that the i-TFC-SG-6 membrane possesses an enhanced antifouling ability. Despite the composite SOD/GO interlayer increases the surface roughness of membrane, it endows the membrane with greater hydrophilic surface, reduced membrane thickness, and shortened water transport pathway, which leads to an enhanced antifouling ability for the i-TFC-SG-6 membrane [61, 62]. Meanwhile, the i-TFC-SG-6 membrane depicts a stable PWP and Na_2SO_4 rejection during the 80 h of filtration (Fig. 10b). In Fig. 10c, a linear relationship with between water flux and operating pressure of i-TFC-SG-6 membrane appeared in the pressure range of 1-9 bar, while the pressure range of the linear relationship for controlled TFC membrane is 1-6 bar. The composite interlayer composing of rigid SOD zeolite and GO nanosheet can improve the mechanical stability of the interface to alleviate the compression,

which endows the membrane with improved pressure resistance [63, 64]. The outstanding performance, excellent antifouling ability, long-term operating stability, and pressure resistance of the i-TFC-SG membrane illustrate its greater potential in practical nanofiltration applications.

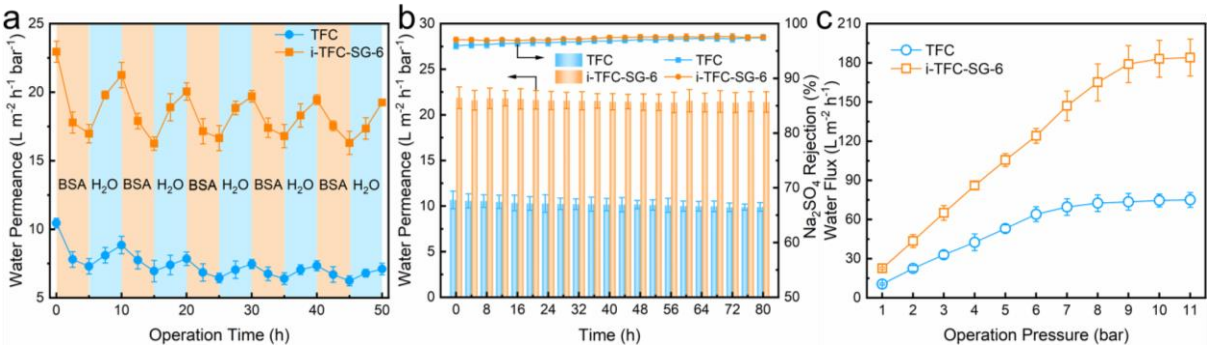

Fig. 10. (a) Time-dependent normalized water flux of TFC and i-TFC-SG-6 membranes with fouling-rinsing cycles with water and BSA solution, (b) Long-term stability test of controlled TFC and i-TFC-SG-6 membranes, (c) Pressure resistance test of TFC and i-TFC-SG-6 membranes

4. Conclusion

In this work, a thinner i-TFC NF membrane was constructed by inserting high-porosity SOD/GO composite materials as an interlayer. The interaction of SOD/GO interlayer with amine monomers and the tortuous effect resulted in significantly slowed diffusion of the amine monomer (reduction of 50% in diffusion rate), which facilitates the homogeneous and controllable IP process. A slow IP process leads to the formation of a thinner PA layer with stripe morphology and narrow pore size, thus achieving a higher water permeance. As the result, the optimal i-TFC-SG-6 membrane achieved a superior water permeance of 22.05 L m^{-2} h^{-1}·bar^{-1} (nearly 2.5-fold to that of the controlled one) and an excellent rejection for Na_2SO_4. Moreover, the interlayer endowed the membranes with excellent antifouling propensity, long-term stability, and pressure resistance. The use of SOD/GO composite interlayer provides a feasible method

411 to control the IP process and regulate the membrane properties precisely.

412 ## Acknowledgements

413 This work was financially supported by National Key Research and Development Program of
414 China of Ministry of Science and Technology (2022YFE0116000), National Natural Science
415 Foundation of China (No. 22175200, No. 21975285), , Fujian Province Science and Technology
416 Program, Innovation Fund (2022C0021), Qingdao Municipal Natural Science Foundation of
417 China (23-2-1-240-zyyd-jch).

418 ## References

419 [1] X. Lu, M. Elimelech, Fabrication of desalination membranes by interfacial polymerization:
420 history, current efforts, and future directions, Chem. Soc. Rev. 50 (22) (2021) 6290-6307.
421 https://doi.org/10.1039/d0cs00502a.
422 [2] W.J. Lau, S. Gray, T. Matsuura, D. Emadzadeh, J. Chen, A.F. Ismail, A review on polyamide
423 thin film nanocomposite (TFN) membranes: History, applications, challenges and
424 approaches, Water Res. 80 (1) (2015) 306-324.
425 https://doi.org/10.1016/j.watres.2015.04.037.
426 [3] S. Guo, Y. Wan, X. Chen, J. Luo, Loose nanofiltration membrane custom-tailored for
427 resource recovery, Chem. Eng. J. 409 (1) (2021) 127376,
428 https://doi.org/10.1016/j.cej.2020.127376.
429 [4] K. Wang, X. Wang, B. Januszewski, Y. Liu, D. Li, R. Fu, M. Elimelech, X. Huang, Tailored
430 design of nanofiltration membranes for water treatment based on synthesis-property-
431 performance relationships, Chem. Soc. Rev. 51 (2) (2021) 672-719.
432 https://doi.org/10.1039/D0CS01599G.
433 [5] Y. Ji, W. Qian, Y. Yu, Q. An, L. Liu, Y. Zhou, C. Gao, Recent developments in nanofiltration
434 membranes based on nanomaterials, Chin. J. Chem. Eng. 25 (11) (2017) 1639-1652.
435 https://doi.org/10.1016/j.cjche.2017.04.014.
436 [6] S. Zhao, C. Ba, Y. Yao, W. Zheng, J. Economy, P. Wang, Removal of antibiotics using
437 polyethylenimine cross-linked nanofiltration membranes, Chem. Eng. J. 335 (1) (2018)
438 101-109, https://doi.org/10.1016/j.cej.2017.10.140.
439 [7] W. J. Lau, A. F. Ismail, N. Misdan, M. A. Kassim, A recent progress in thin film composite

membrane: A review, Desalination 287 (2012) 190-199. https://doi.org/10.1016/j.desal.2011.04.004.

[8] J.M. Gohil, P. Ray, A review on semi-aromatic polyamide TFC membranes prepared by interfacial polymerization: Potential for water treatment and desalination, Sep. Purif. Technol. 181 (30) (2017) 159-182, https://doi.org/10.1016/j.seppur.2017.03.020.

[9] H. B. Park, J. Kamcev, L. M. Robeson, M. Elimelech, B. D. Freeman, Maximizing the right stuff: The trade-off between membrane permeability and selectivity, Science 356 (6343) eaa0530. https://doi.org/10.1126/science.aab0530.

[10] C. Ji, Z. Zhai, C. Jiang, P. Hu, S. Zhao, S. Xue, Z. Yang, T. He, Q. J. Niu, Recent advances in high-performance TFC membranes: A review of the functional interlayers, Desalination 500 (15) (2021) 114869. https://doi.org/10.1016/j.desal.2020.114869.

[11] G. Xu, Z. An, M. Wang, K. Xu, H. Zhao, Q. Liu, Polyamide layer modulation for PA-TFC membranes Optimization: Developments, Mechanisms, and implications, Sep. Purif. Technol. 311 (15) (2023) 123200. https://doi.org/10.1016/j.seppur.2023.123200.

[12] B. Yuan, S. Zhao, P. Hu, J. Cui, Q.J. Niu, Asymmetric polyamide nanofilms with highly ordered nanovoids for water purification, Nat. Commun. 11 (1) (2020) 6102. https://doi.org/10.1038/s41467-020-19809-3.

[13] H. Peng, W. Zhang, W. Hung, N. Wang, J. Sun, K.R. Lee, Q. An, C. Liu, Q. Zhao, Phosphonium Modification Leads to Ultrapermeable Antibacterial Polyamide Composite Membranes with Unreduced Thickness, Adv. Mater. 32 (23) (2020) 2001383, https://doi.org/10.1002/adma.202001383.

[14] B. Yuan, C. Jiang, P. Li, H. Sun, T. Yuan, H. Sun, Q. Niu, Ultrathin polyamide membrane with decreased porosity designed for outstanding water-softening performance and superior antifouling properties, Acs Appl. Mater. Inter. 10 (49) (2018) 43057-43067, https://doi.org/10.1021/acsami.8b15883.

[15] J. Ding, H. Wu, P. Wu, Preparation of highly permeable loose nanofiltration membranes using sulfonated polyethylenimine for effective dye/salt fractionation, Chem. Eng. J. 396 (15) (2020) 125199, https://doi.org/10.1016/j.cej.2020.125199.

[16] S. Xiong, S. Xu, A. Phommachanh, M. Yi, Y, Wang, Versatile Surface Modification of TFC Membrane by Layer-by-Layer Assembly of Phytic Acid-Metal Complexes for Comprehensively Enhanced FO Performance, Environ. Sci. Technol. 53 (6) (2019) 3331-3341. https://doi.org/10.1021/acs.est.8b06628.

[17] Y.S. Khoo, W.J. Lau, Y.Y. Liang, N. Yusof, A.F. Ismail, Surface modification of PA layer of TFC membranes: Does it effective for performance Improvement?, J. Ind. Eng. Chem.

102 (25) (2021) 271-292. https://doi.org/10.1016/j.jiec.2021.07.006.
[18]S. Xu, Q. Shen, L. Luo, Y. Tong, Y. Wu, Z. Xu, H. Zhang, Surfactants attached thin film composite (TFC) nanofiltration (NF) membrane via intermolecular interaction for heavy metals removal, J. Membr. Sci. 642 (15) (2022) 119930, https://doi.org/10.1016/j.memsci.2021.119930.
[19]J. Wang, Z. Wang, Y. Liu, J. Wang, S. Wang, Surface modification of NF membrane with zwitterionic polymer to improve anti-biofouling property, J. Membr. Sci. 514 (15) (2016) 407-417, https://doi.org/10.1016/j.memsci.2016.05.014.
[20]H. Feng, K. Yuan, Y. Liu, B. Luo, Q. Wu, X. Bao, W. Wei, J. Ma, Recent advances in covalent organic framework-based membranes for water purification: Insights into separation mechanisms and applications, Chem. Eng. J. 474 (15) (2023) 145580, https://doi.org/10.1016/j.cej.2023.145580.
[21]X. Wu, L. Yang, F. Meng, W. Shao, X. Liu, M. Li, ZIF-8-incorporated thin-film nanocomposite (TFN) nanofiltration membranes: Importance of particle deposition methods on structure and performance, J. Membr. Sci. 632 (15) (2021) 119356, https://doi.org/10.1016/j.memsci.2021.119356.
[22]L. Bai, Y. Liu, A. Ding, N. Ren, G. Li, H. Liang, Fabrication and characterization of thin-film composite (TFC) nanofiltration membranes incorporated with cellulose nanocrystals (CNCs) for enhanced desalination performance and dye removal, Chem. Eng. J. 358 (15) (2019) 1519-1528, https://doi.org/10.1016/j.cej.2018.10.147.
[23]Q. Xie, S. Zhang, Z. Hong, H. Ma, B. Zeng, X. Gong, W. Shao, Q. Wang, A novel double-modified strategy to enhance the performance of thin-film nanocomposite nanofiltration membranes: Incorporating functionalized graphenes into supporting and selective layers, Chem. Eng. J. 368 (15) (2019) 186-201, https://doi.org/10.1016/j.cej.2019.02.180.
[24]D. Yadav, S. Karki, M.B. Gohain, P.G. Ingole, Development of micropollutants removal process using thin-film nanocomposite membranes prepared by green new vapour-phase interfacial polymerization method, Chem. Eng. J. 472 (15) (2023) 144940, https://doi.org/10.1016/j.cej.2023.144940.
[25]Q. Peng, Y. Lu, W. Fang, Y. Zhu, J. Jin, Attenuated thermal-regulated interfacial polymerization towards polyamide nanofiltration membrane with unprecedentedly enhanced performance, Chem. Eng. J. 471 (1) (2023) 144706, https://doi.org/10.1016/j.cej.2023.144706.
[26]C. Ge, M. Sheng, Y. Yuan, F. Shi, Y. Yang, S. Zhao, J. Wang, Z. Wang, Recent advances of the interfacial polymerization process in gas separation membranes fabrication, J. Membr.

Sci. 683 (5) (2023) 121854, https://doi.org/10.1016/j.memsci.2023.121854.

[27] S. Han, J. Zhu, A.A. Uliana, D. Li, Y. Zhang, L. Zhang, Y. Wang, T. He, M. Elimelech, Microporous organic nanotube assisted design of high performance nanofiltration membranes, Nat. Commun. 13 (1) (2022) 7954. https://doi.org/10.1038/s41467-022-35681-9.

[28] S. Xu, H. Lin, G. Li, J. Wang, Q. Han, F. Liu, Anionic covalent organic framework as an interlayer to fabricate negatively charged polyamide composite nanofiltration membrane featuring ions sieving, Chem. Eng. J. 427 (1) (2022) 132009, https://doi.org/10.1016/j.cej.2021.132009.

[29] X. Wang, Q. Xiao, C. Wu, P. Li, S. Xia, Fabrication of nanofiltration membrane on MoS2 modified PVDF substrate for excellent permeability, salt rejection, and structural stability, Chem. Eng. J. 416 (15) (2021) 129154, https://doi.org/10.1016/j.cej.2021.129154.

[30] R. Dai, J. Li, Z. Wang, Constructing interlayer to tailor structure and performance of thin-film composite polyamide membranes: A review, Adv. Colloid Interface Sci., 282 (2020) 102204. https://doi.org/10.1016/j.cis.2020.102204.

[31] X. Liu, Y, Cao, Y. Li, Z. Xu, Z. Li, M. Wang, X. Ma, High-performance polyamide/ceramic hollow fiber TFC membranes with TiO2 interlayer for pervaporation dehydration of isopropanol solution, J. Membr. Sci. 576 (15) (2019) 26-35. https://doi.org/10.1016/j.memsci.2019.01.023.

[32] M. Chi, P. Zheng, M. Wei, A. Zhu, L. Zhong, Q. Zhang, Q. Liu, Polyamide composite nanofiltration membrane modified by nanoporous TiO_2 interlayer for enhanced water permeability, J. Ind. Eng. Chem. 115 (25) (2022) 230-240, https://doi.org/10.1016/j.jiec.2022.08.004.

[33] M. Wu, Y. Lv, H. Yang, L. Liu, X. Zhang, Z. Xu, Thin film composite membranes combining carbon nanotube intermediate layer and microfiltration support for high nanofiltration performances, J. Membr. Sci. 515 (1) (2016) 238-244. https://doi.org/10.1016/j.memsci.2016.05.056.

[34] G. Gong, P. Wang, Z. Zhou, Y. Hu, New Insights into the Role of an Interlayer for the Fabrication of Highly Selective and Permeable Thin-Film Composite Nanofiltration Membrane, ACS Appl. Mater. Interfaces, 11 (7) (2019) 7349-7356, https://doi.org/10.1021/acsami.8b18719.

[35] X. Song, Y. Zhang, H.M. Abdel-Ghafar, E.S.A Abdel-Asl, M. Huang, S. Gui, H. Jiang,

Polyamide membrane with an ultrathin GO interlayer on macroporous substrate for minimizing internal concentration polarization in forward osmosis, Chem. Eng. J. 412 (15) (2021) 128607. https://doi.org/10.1016/j.cej.2021.128607.

[36] G.S. Lai, W.J. Lau, P.S. Goh, A.F. Ismail, Y.H. Tan, C.Y. Chong, R. Krause-Rehberg, S. Award, Tailor-made thin film nanocomposite membrane incorporated with graphene oxide using novel interfacial polymerization technique for enhanced water separation, Chem. Eng. J. 344 (15) (2018) 524-534, https://doi.org/10.1016/j.cej.2018.03.116.

[37] D. Zhao, F. Fang, L. Shen, Z. Huang, Q. Zhao, H. Lin, T. Chung, Engineering metal–organic frameworks (MOFs) based thin-film nanocomposite (TFN) membranes for molecular separation, Chem. Eng. J. 454 (3, 15) (2023) 1404747, https://doi.org/10.1016/j.cej.2022.140447.

[38] X. Jin, X. Liang, J. Liu, J. Mo, T. Ren, X. Ma, Z. Xu, Development of high permeability nanofiltration membranes through porous 2D MOF nanosheets, Chem. Eng. J. 471 (1) (2023) 144566, https://doi.org/10.1016/j.cej.2023.144566.

[39] S. Wei, Y. Guo, G. Yang, H. Guo, Z. Yan, S. Mintova, Q.J. Niu, EMT-NH_2 zeolite interlayer induces the formation of high-performance polyamide membrane, Chem. Eng. J. 472 (15) (2023) 145081, https://doi.org/10.1016/j.cej.2023.145081.

[40] B. Li, Z. Yang, Y. Dou, J. Zhang, J. Lu, J. Han, Two-Dimensional LDH Film Templating for Controlled Preparation and Performance Enhancement of Polyamide Nanofiltration Membranes, Angew. Chem. Int. Ed. 62 (2023) e202304442. https://doi.org/10.1002/anie.202304442.

[41] S. Wang, L. Yang, G. He, B. Shi, Y. Li, H. Wu, R. Zhang, S. Nunes, Z. Jiang, Two-dimensional nanochannel membranes for molecular and ionic separations, Chem. Soc. Rev. 49 (4) (2020) 1071-1089. https://doi.org/10.1039/c9cs00751b.

[42] M. Liu, D.C.C. Femandes, Z.S.S.L. Saleeba, R.H. Hurt, Controlled Release of Molecular Intercalants from Two-Dimensional Nanosheet Films, ACS Nano 16 (4) 6941, https://doi.org/10.1021/acsnano.2c02972.

[43] S. Zhou, K. Guan, Z. Wang, Q. Song, Z. Li, P. Xu, L. Deng, S. Xiang, H. Matsuyama, Confined and mediated intercalation of nanoparticles in graphene oxide membrane to fine-tune desalination performance, Chem. Eng. J. 465 (1) (2023) 143005, https://doi.org/10.1016/j.cej.2023.143005.

[44] L. Tian, Y. Jiang, S. Li, L. Han, B. Su, Graphene oxide interlayered thin-film nanocomposite hollow fiber nanofiltration membranes with enhanced aqueous electrolyte separation performance, Sep. Purif. Technol. 248 (1) (2020) 117153,

https://doi.org/10.1016/j.seppur.2020.117153.
[45] Y. Wei, Y. Zhu, Y, Jiang, Photocatalytic self-cleaning carbon nitride nanotube intercalated reduced graphene oxide membranes for enhanced water purification, Chem. Eng. J. 365 (15) (2019) 915-926, https://doi.org/10.1016/j.cej.2018.09.108.
[46] L. Yang, X. Xiao, S. Shen, J. Lama, M. Hu, F. Jia, Z. Han, H. Qu, L. Huang, Y. Wang, Recent Advances in Graphene Oxide Membranes for Nanofiltration, ACS Appl. Nano Mater. 5 (3) (2022) 3121-3145, https://doi.org/10.1021/acsanm.1c04469.
[47] Z. Liao, J. Zhu, X. Li, B. van der Bruggen, Regulating composition and structure of nanofillers in thin film nanocomposite (TFN) membranes for enhanced separation performance: A critical review, Sep. Purif. Technol. 266 (1) (2021) 118567, https://doi.org/10.1016/j.seppur.2021.118567.
[48] B. Borjigin, L. Liu, L. Yu, L. Xu, C. Zhao, J. Wang, Influence of incorporating beta zeolite nanoparticles on water permeability and ion selectivity of polyamide nanofiltration membranes, J. Environ. Sci. 98 (2020) 77-84, https://doi.org/10.1016/j.jes.2020.04.010.
[49] N. Ghaemi, P. Safari, Nano-porous SAPO-34 enhanced thin-film nanocomposite polymeric membrane: Simultaneously high water permeation and complete removal of cationic/anionic dyes from water, J. Hazard. Mater. 358 (15) (2018) 376-388, https://doi.org/10.1016/j.jhazmat.2018.07.017.
[50] G. Kong, L. Fan, L. Zhao, Y. Feng, X. Cui, J. Pang, H. Guo, H. Sun, Z. Kang, D. Sun, S. Mintova, Spray-dispersion of ultra-small EMT zeolite crystals in thin-film composite membrane for high-permeability nanofiltration process, J. Membr. Sci. 622 (15) (2021) 119045, https://doi.org/10.1016/j.memsci.2020.119045.
[51] G. Yang, H, Guo, Z. Kang, S. Feng, L. Zhao, S. Mintova, Sandwich-type H2/CO2 membranes comprising of graphene oxide and sodalite crystals with adjustable morphology and size, Microporous Mesoporous Mater. 300 (15) (2020) 110020, https://doi.org/10.1016/j.micromeso.2020.110120.
[52] H. Guo, G. Kong, G. Yang, J. Pang, Z. Kang, S. Feng, L. Zhao, L. Fan, L. Zhu, A. Vicente, P. Peng, Z. Yan, D. Sun, S. Mintova, Cross-Linking between Sodalite Nanoparticles and Graphene Oxide in Composite Membranes to Trigger High Gas Permeance, Selectivity, and Stability in Hydrogen Separation, Angew. Chem. Int. Ed. 59 (15) (2020) 6284-6288. https://doi.org/10.1002/anie.201915797.
[53] S. Mintova, J. Maguy, V. Valtchev, Nanosized microporous crystals: emerging applications, Chem. Soc. Rev. 44 (2015) 7207-7233. https://doi.org/10.1039/c5cs00210a.
[54] S. Singh, K.C. Khulbe, T. Matsuura, P. Ramamurthy, Membrane characterization by solute

608 transport and atomic force microscopy, J. Membr. Sci. 142 (1/2) (1998) 111-127,
609 https://doi.org/10.1016/S0376-7388(97)00329-3.
610 [55]Ge. Yang, H. Guo, Z. Kang, L. Zhao, S. Feng, F. Jiao, S. Mintova, Green Hydrogen
611 Separation from Nitrogen by Mixed-Matrix Membranes Consisting of Nanosized Sodalite
612 Crystals, ChemSusChem 12 (19) (2018) 1529-4537,
613 https://doi.org/10.1002/cssc.201802577.
614 [56]I.C. Medeiros-Costa, E. Dib, N. Nesterenko, J.P. Dath, J.P. Gilson, S. Mintova, Silanol
615 defect engineering and healing in zeolites: opportunities to fine-tune their properties and
616 performances, Chem. Soc. Rev. 50 (19) (2021) 11156-11179,
617 https://doi.org/10.1039/d1cs00395j.
618 [57]W, Zeng, C. Li, Y. Feng, S. Zeng, B. Fu, X. Zhang, Carboxylated multi-walled carbon
619 nanotubes (MWCNTs-COOH)-intercalated graphene oxide membranes for highly efficient
620 treatment of organic wastewater, J. Water Process. Eng. 40 (2021) 101901,
621 https://doi.org/10.1016/j.jwpe.2020.101901.
622 [58]V. Freger, Nanoscale Heterogeneity of Polyamide Membranes Formed by Interfacial
623 Polymerization, Langmuir 19 (11) (2003) 4791-4797, http://dx.doi.org/10.1021/la020920q.
624 [59]L. Bai, Y. Liu, N. Bossa, A. Ding, N. Ren, G. Li, H. Liang, M.R. Wisener, Incorporation
625 of Cellulose Nanocrystals (CNCs) into the Polyamide Layer of Thin-Film Composite (TFC)
626 Nanofiltration Membranes for Enhanced Separation Performance and Antifouling
627 Properties, Environ. Sci. Technol. 51 (19) (2018) 11178-11187,
628 https://doi.org/10.1021/acs.est.8b04102.
629 [60]H. Saleem, S.J. Zaidi, Nanoparticles in reverse osmosis membranes for desalination: A state
630 of the art review, Desalination 451 (1) (2020) 114171,
631 https://doi.org/10.1016/j.desal.2019.114171.
632 [61]D. Rana, T. Matsuura, Surface Modifications for Antifouling Membranes, Chem. Rev. 110
633 (4) (2010) 2448-2471. https://doi.org/10.1021/cr800208y.
634 [62]Q. Gan, C. Wu, L. Long, l.E. Peng, Z. Yang, H. Guo, C.Y.Y. Tang, Does Surface Roughness
635 Necessarily Increase the Fouling Propensity of Polyamide Reverse Osmosis Membranes
636 by Humic Acid?, Environ. Sci. Technol. 57 (6) (2023) 1548-2556,
637 https://doi.org/10.1021/acs.est.2c07872.
638 [63]M. Yasukawa, S. Mishima, Y. Tanaka, T. Takahashi, H. Matsuyama, Thin-film composite
639 forward osmosis membrane with high water flux and high pressure resistance using a
640 thicker void-free polyketone porous support, Desalination 402 (16) (2017) 1-9,
641 https://doi.org/10.1016/j.desal.2016.09.017.

642 [64]S. Xue, C. Lin, C. Ji, Y. Guo, L. Liu, Z. Yang, S. Zhao, X. Cai, Q.J. Jason, R.B. Kaner,
643 Thin-Film Composite Membranes with a Hybrid Dimensional Titania Interlayer for
644 Ultrapermeable Nanofiltration, Nano Letter 22 (3) (2022) 1039–1046, https://doi.
645 org/10.1021/acs.nanolett.1c04000.